A simple particle–spring method for capturing the continuous–discontinuous processes of brittle materials

Chun Feng [a,b,*], Xinming Liu [a,c], Qindong Lin [d], Shihai Li [a]

[a] *Key Laboratory for Mechanics in Fluid Solid Coupling Systems, Institute of Mechanics, Chinese Academy of Sciences, Beijing, China*
[b] *International Centre for Numerical Methods in Engineering (CIMNE), Universitat Politècnica de Catalunya, Barcelona, Spain*
[c] *School of Engineering Science, University of Chinese Academy of Sciences, Beijing 100049, China*
[d] *Xi'an Modern Chemistry Research Institute, Xi'an, Shanxi, 710065, China*

ARTICLE INFO

ABSTRACT

Comparing to the continuum-based method such as the finite element method (FEM), particle–spring method can relatively easily simulate the cracking processes of brittle materials such as rocks by deactivating or adjusting springs/contacts. However, it is still challenging for building the equivalence between particle–spring system and the original continuous media, then capturing the whole continuous–discontinuous processes. In this work, a simple particle–spring system is proposed in which different types of springs are introduced including normal, tangential, pure shearing and Poisson's springs. The stiffness of the springs are obtained by bridging the proposed model and triangular FEM element. Moreover, novel mixed type failure criteria for the breakage of the springs are also provided. By numerical studies the reliability and robustness of the model are proven which gives comparable results to the conventional FEM model. With the new model, progressive failure processes of rock-like material can be properly captured.

1. Introduction

Failure processes of brittle materials such as rocks, ceramics are characterized by suddenness and considerable strain softening, which is accompanied by strong discontinuities and high localization [1,2].

Many sophisticated numerical models are presented in the last decades, either in a continuum or discrete framework [2–4]. For example, in the framework of Finite Element Method (FEM), some models smear the crack across several elements with limited width [5–8]. Some combine interface elements and remeshing techniques [9,10]. Some use nodal or elemental enrichments such as Extended Finite Element Method (XFEM) [11–15], Numerical Manifold Method [16–20], Strong Discontinuity embedded Approach (SDA) [21–24] and Cracking Elements (CE) [25–29]. These models mostly consider the domains with and without cracks are different, which shall be modeled with different methods. When multiple cracks appear, complex strategies such as crack tracking [30–32], multiple remeshing [33,34] and complicated enrichments [35,36] or mathematical covers could be inevitable, bringing computing efforts.

On the other hand, when modeling a continuous media with discrete particles, the cracking processes can be modeled by breaking the connections of particles, which could be numerically more efficient. Such approaches include classic meshfree models [37–40],

Cracking particles [41–44], lattice elements [45–47] and peridynamic models [48–51]. Recently, the dual-horizon peridynamics and the Nonlocal Operator Method (NOM) show great potential in modeling complex fracture. These two methods inherit the advantages of PD in modeling fracture, but allow for adaptive refinement and modeling coupled problems. The dual-horizon peridynamics [52,53] optimizes the requirements for horizon-size and regular particle discretization, and improves computational efficiency greatly. NOM [54,55] does not require shape functions and has high-order continuity for solving higher-order problems. In addition, Particle Discrete Element Method (PDEM) is a widely used particle–spring method [56,57]. Based on the force-chain crack model [58], the spring element method (SEM) [59, 60] is developed to describe the deformation of continuous solid media. Extend Discrete Element Method (EDEM) [61] can describe the process of crack propagation and fracture of concrete members. The Applied Element Method (AEM) [62] assumes that the micro-element body is rigid and all the deformation is concentrated on the connecting spring between the micro-elements, which can accurately describe the propagation of cracks. The challenges of particles methods include: (i) efficiently build equivalence between the particle–spring and the original continuum domain, (ii) equivalent failure criterion for the springs.

This work proposes a novel particle–spring method. Several types of springs are introduced for accounting the mechanical responses of continuum media, such as normal, tangential, pure shearing and Poisson's effects. The stiffness of the springs are obtained by considering the stiffness of corresponding FEM grids with simple and efficient numerical procedures. A failure criterion is also built by taking into account the particle stress and contact areas. Several numerical examples reproducing indoor experiments are provided for demonstrating the reliability of the model which is very suitable for simulating rock failure.

The remaining parts of the paper are organized as follows: In Section 2, the particle–spring method is proposed including the new spring system for accounting the mechanical responses of continuous material. The stiffness matrix are deduced and provided in details. Then, mixed type failure criteria are given, taking into account tensile and compressive-shear failures. In Section 3, several numerical examples are given. The continuous and discontinuous behaviors of rock-like material are simulated by the proposed method, comparing to the FEM results. The paper closes with concluding remarks given in Section 4.

2. The model

2.1. Equivalence of continuum and particle–spring systems

In order to correctly describe the mechanical response of continuous medium materials, it is necessary to ensure that the total energy of the particle–spring system is equal to that of the continuous medium. For solving the deformation problem of continuous linear elastic medium under given boundary conditions, the material deforms under external load, and the external force work is equal to the deformation energy stored in continuous medium. Therefore, the particle–spring method requires that the elastic potential energy of the spring system is equal to the elastic strain energy of the continuum. On the constructed particle–spring system, the expression of spring stiffness in a specific spring system can be obtained by variation of elastic strain energy of continuum. The deformation energy of the continuous media and particle–spring system could represent as

$$\Pi_c = \int \frac{1}{2} \sigma_{ij} \varepsilon_{ij} dV \tag{1}$$

$$\Pi_d = \sum_{i=1}^{N} K_i \Delta u_i \tag{2}$$

where, Π_c and Π_d denote the deformation energy of continuous media and particle–spring system respectively, λ and G are Lame constants and shear modulus, θ and ε_{ij} means the bulk strain and strain tensor, and δ_{ij} is Kronecker delta. For isotropic linear elastic continuous media, c could be expressed as

$$\Pi_c = \int \frac{1}{2} (\lambda \theta \delta_{ij} + 2G \varepsilon_{ij}) \varepsilon_{ij} dV \tag{3}$$

To ensure the equivalence of these two deformation energies, Eq. (4) should be satisfied.

$$\Pi_c = \Pi_d \tag{4}$$

By comparison each component in Eq. (4), the stiffness of each spring in particle–spring system could be obtained. According to the construction procedure of particle–spring system, it is easy to extend this method to higher order elements or three dimensional elements, and it is also easy to deal with anisotropic elasticity, nonlinear material behavior. Here, we take linear elastic constant strain triangular finite element for an example. Considering the continuum system, each element owns its stiffness matrix, which is built based on the material and geometric properties. With the stiffness matrix $\mathbf{K}_{fem}$, the linear elastic relationship accounting the nodal forces $\mathbf{F}$ and displacements $\mathbf{U}$ can be obtained

$$\mathbf{F} = \mathbf{K}_{fem} \mathbf{U} \tag{5}$$
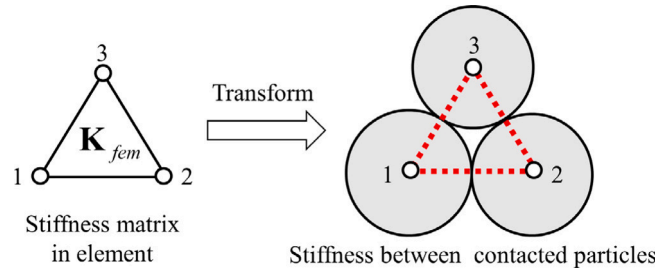

Fig. 1. Stiffness transform from finite element to particle–spring system.

On the other side, considering a particle–spring system, each contact pair is composed by two particles. The force and displacement relationship of this pair is controlled by normal and tangential springs connecting the two particles as

$$\begin{cases} F_n = K_n \Delta u_n \\ F_t = K_t \Delta u_t \end{cases} \tag{6}$$

where F_n and F_s denote normal tangential contact forces, K_n and K_r are the corresponding normal and tangential stiffness, Δu_n and Δu_r denote the normal tangential relative displacements between the contacted particles. When properly transmitting $\mathbf{K}_{fem}$ into K_n, a constant strain particle–spring system can also represent a continuum system, see Fig. 1.

Different from traditional DEM, in particle–spring method, the contact pairs are constructed via finite elements, shown in Fig. 2. Firstly, a tightly packed particle system is created by particle generation algorithm. Then, by treating centroid of particles as the nodes of the elements, triangular finite elements are constructed by Delaunay method. At last, by considering the edges of the finite elements as the contact bond, the contact pairs for each particle are created.

The mass of each particle in particle–spring system is computed by corresponding triangular finite elements, as

$$m_i = \sum_{j=1}^{N} \rho_j S_j t / 3 \tag{7}$$

where, m_i is the mass of ith particle, ρ_j and S_j are the density and area of jth triangular element related to ith particle, and t is the thickness (1.0 m is adopted in this paper). In elastic stage, with the appropriate spring stiffness, the particle–spring could represent feature of continuous media. Once the particle spring failure, the mesoscopic effect will appear, and the particle shape and particle configuration will affect the result greatly.

2.2. Equivalent spring system

For building the equivalent spring system. A linear triangular finite element with arbitrary shape is shown in Fig. 3, with three nodes 1(0,0), 2(b,0), 3(c,w), respectively. The corresponding three edges are denoted as d_{12}, d_{23} and d_{13}. Then, three other nodes are introduced as the intersection points of the altitudes and the edges as nodes 4, 5 and 6. The altitudes are denoted as h_{34}, h_{26} and h_{15}. The polar angles of d_{23}, d_{13}, h_{26} and h_{15} to the x-axis are $\hat{\alpha}$, $\hat{\beta}$, $\hat{\gamma}$ and $\hat{\omega}$.

Then, for a corresponding particle–spring system, totally nine springs are introduced including three conventional springs and six unconventional springs, see Fig. 4. Each conventional spring has normal and tangential components, where the force and deformation are
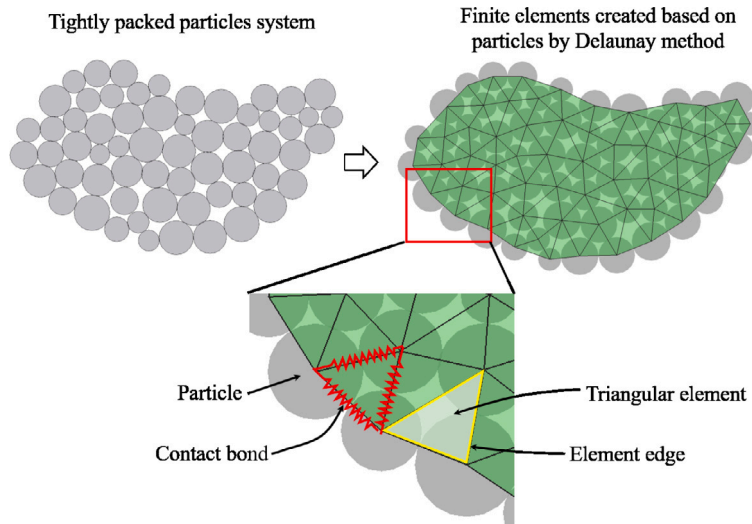
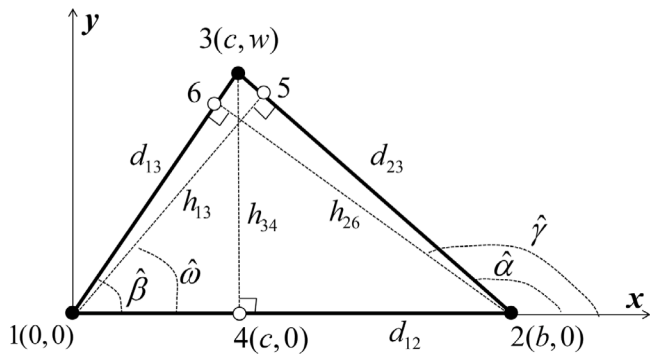**Fig. 2.** Construction of particle–spring system.

Fig. 3. Triangular element in the local coordinate system.

controlled by linear elastic relationship:

$$\begin{cases} F_{1n} = k_{1n}(u_2 - u_1) \\ F_{1s} = k_{1s}(v_2 - v_1) \\ F_{2n} = k_{2n}\left[(u_3 - u_2)\cos\alpha + (v_3 - v_2)\sin\alpha\right] \\ F_{2s} = k_{2s}\left[-(u_3 - u_2)\sin\alpha + (v_3 - v_2)\cos\alpha\right] \\ F_{3n} = k_{3n}\left[(u_1 - u_3)\cos\beta + (v_1 - v_3)\sin\beta\right] \\ F_{3s} = k_{3s}\left[-(u_1 - u_3)\sin\beta + (v_1 - v_3)\cos\beta\right] \end{cases} \quad (8)$$

where $F_{1n} \sim F_{3n}$ and $F_{1s} \sim F_{3s}$ denote normal and tangential forces of springs $s_1 - s_3$ respectively. $k_{1n} \sim k_{3n}$ and $k_{1s} \sim k_{3s}$ denote normal and tangential stiffnesses of springs $s_1 - s_3$ respectively. u and v denote node displacements in x and y directions. α and β denote position angles, obtained by

$$\begin{cases} \alpha = \hat{\alpha} \\ \beta = \hat{\beta} + 180° \end{cases} \quad (9)$$

Each unconventional spring contain also two stiffness components as Poisson's stiffness and pure shearing stiffness. Poisson's stiffness is introduced for accounting the Poisson effect and pure shearing stiffness is used for accounting the momentum effect of continuous media. The

spring forces are determined by

$$\begin{cases} F_{4n} = K_p^{xy}(v_3 - v_4) \\ F_{4s} = K_s^{xy}(u_3 - u_4) \\ F_{5n} = K_p^{xy}(u_2 - u_1) \\ F_{5s} = K_s^{xy}(v_2 - v_1) \\ F_{6n} = K_p^{xy}\left[(u_1 - u_5)\cos\omega + (v_1 - v_5)\sin\omega\right] \\ F_{6s} = K_s^{xy}\left[-(u_1 - u_5)\sin\omega + (v_1 - v_5)\cos\omega\right] \\ F_{7n} = K_p^{xy}\left[(u_3 - u_2)\cos\alpha + (v_3 - v_2)\sin\alpha\right] \\ F_{7s} = K_s^{xy}\left[-(u_3 - u_2)\sin\alpha + (v_3 - v_2)\cos\alpha\right] \\ F_{8n} = K_p^{xy}\left[(u_2 - u_6)\cos\gamma + (v_2 - v_6)\sin\gamma\right] \\ F_{8s} = K_s^{xy}\left[-(u_2 - u_6)\sin\gamma + (v_2 - v_6)\cos\gamma\right] \\ F_{9n} = K_p^{xy}\left[(u_1 - u_3)\cos\beta + (v_1 - v_3)\sin\beta\right] \\ F_{9s} = K_s^{xy}\left[-(u_1 - u_3)\sin\beta + (v_1 - v_3)\cos\beta\right] \end{cases} \quad (10)$$

where K_p^{xy} and K_s^{xy} are the Poisson's and pure shear stiffnesses. u_4, v_4, u_5, v_5, u_6 and v_6 are the displacements of interpolated nodes 4, 5 and 6. γ and ω are determined by

$$\begin{cases} \gamma = -\hat{\gamma} \\ \omega = \hat{\omega} + 180° \end{cases} \quad (11)$$

Nodes 4, 5 and 6 lie on the edges, which are interpolated points of nodes 1, 2 and 3. Hence, their displacements can be determined by

$$\begin{cases} u_4 = N_4^1 u_1 + N_4^2 u_2 & v_4 = N_4^1 v_1 + N_4^2 v_2 \\ u_5 = N_5^1 u_2 + N_5^2 u_3 & v_5 = N_5^1 v_2 + N_5^2 v_3 \\ u_6 = N_6^1 u_1 + N_6^2 u_3 & v_6 = N_6^1 v_1 + N_6^2 v_3 \end{cases} \quad (12)$$

where N_4^1, N_4^2, N_5^1, N_5^2, N_6^1 and N_6^2 are the interpolation coefficients.

It is worth mentioning that for unconventional springs the direction of deformations and the direction of forces are perpendicular to each other. For example, spring 4 shown in Fig. 4(b) is introduced for providing the normal force between nodes 1 and 2 generated by the relative normal displacement of nodes 3 and 4 (Poisson's effect) and tangential force between nodes 1 and 2 generated by the tangential displacement of nodes 3 and 4 (pure shearing effect).

In Eqs. (8)~(10) and (12)~(17), there are eight indeterminate stiffness coefficients, including three normal stiffness coefficients $k_{1n} \sim k_{3n}$, three tangential stiffness coefficients $k_{1s} \sim k_{3s}$, one Poisson's stiffness coefficient K_p^{xy} and one pure shearing stiffness coefficient K_s^{xy}.
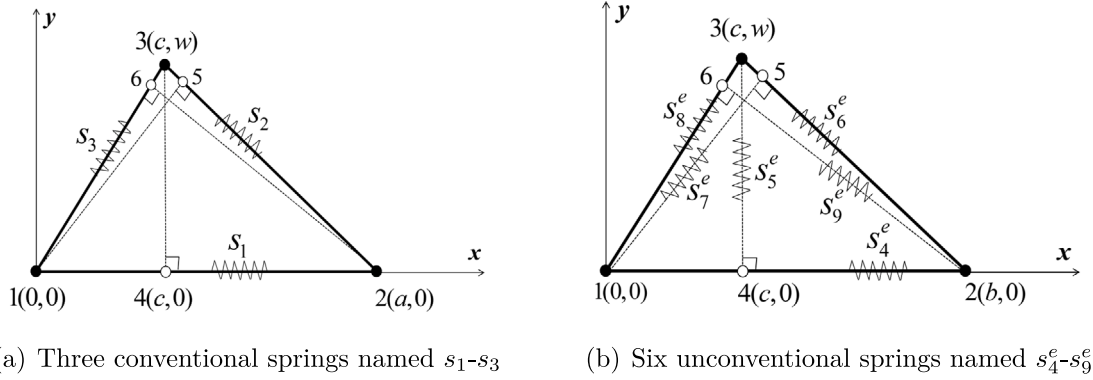
(a) Three conventional springs named s_1-s_3

(b) Six unconventional springs named s_4^e-s_9^e

Fig. 4. Equivalent spring system.

2.3. Spring stiffness coefficients

The deformation energy function is

$$E_d = \frac{1}{2} \left\{ \begin{array}{l} k_{1n}(u_2 - u_1)^2 + k_{1s}(v_2 - v_1)^2+ \\ k_{2n}[(u_3 - u_2)\cos\alpha + (v_3 - v_2)\sin\alpha]^2+ \\ k_{2s}[-(u_3 - u_2)\sin\alpha + (v_3 - v_2)\cos\alpha]^2+ \\ k_{3n}[(u_1 - u_3)\cos\beta + (v_1 - v_3)\sin\beta]^2+ \\ k_{3s}[-(u_1 - u_3)\sin\beta + (v_1 - v_3)\cos\beta]^2+ \\ 2K_p^{xy}(u_2 - u_1)(v_3 - v_4)+ \\ 2K_s^{xy}(u_3 - u_4)(v_2 - v_1)+ \\ 2K_p^{xy}[(u_1 - u_5)\cos\omega + (v_1 - v_5)\sin\omega][(u_3 - u_2)\cos\alpha+ \\ (v_3 - v_2)\sin\alpha]+ \\ 2K_s^{xy}[-(u_1 - u_5)\sin\omega + (v_1 - v_5)\cos\omega][-(u_3 - u_2)\sin\alpha+ \\ (v_3 - v_2)\cos\alpha]+ \\ 2K_p^{xy}[(u_2 - u_6)\cos\gamma + (v_2 - v_6)\sin\gamma][(u_1 - u_3)\cos\beta+ \\ (v_1 - v_3)\sin\beta]+ \\ 2K_s^{xy}[-(u_2 - u_6)\sin\gamma + (v_2 - v_6)\cos\gamma][-(u_1 - u_3)\sin\beta+ \\ (v_1 - v_3)\cos\beta] \end{array} \right\} \quad (13)$$

Based on the functional variation to node displacements u_1, v_1, u_2, v_2, u_3 and v_3, the relationship between node forces and node displacements for the triangular-shaped particle–spring system is obtained (Eq. (9)).

$$\mathbf{F} = \mathbf{K}_{sp}\mathbf{u} \quad (14)$$

where $\mathbf{K}_{sp}$ is a 6×6 stiffness matrix of the equivalent particle–spring system containing 8 indeterminate stiffness coefficients. By comparing $\mathbf{K}_{sp}$ and $\mathbf{K}_{fem}$ in Eq. (5), the 8 stiffness coefficients can be obtained. Considering plane stress conditions, the stiffness coefficients for equilateral triangle are

$$\begin{cases} k_{1n} = k_{2n} = k_{3n} = \dfrac{1}{3}\dfrac{Et}{(1-v^2)}\dfrac{h}{d} \\[2mm] k_{1s} = k_{2s} = k_{3s} = \dfrac{1}{3}\dfrac{Et}{2(1+v)}\dfrac{h}{d} \\[2mm] K_p^{xy} = \dfrac{1}{3}\dfrac{vEt}{2(1-v^2)} \\[2mm] K_s^{xy} = \dfrac{1}{3}\dfrac{Et}{4(1+v)} \end{cases} \quad (15)$$

where E and v denote elastic modulus and Poisson's ratio, t denotes thickness, d and h denote the edge and altitude lengths. For arbitrary

shaped triangular element, the approximate solution is provided as

$$\begin{cases} k_{1n} = \dfrac{1}{2}\dfrac{Et}{(1-v^2)}\dfrac{h_{34}}{d_{12}}\left[\dfrac{1}{3} + \dfrac{d_{13}d_{23}}{(d_{12} + d_{13} + d_{23})d_{12}}\right] \\[3mm] k_{1s} = \dfrac{1}{2}\dfrac{Et}{2(1+v)}\dfrac{h_{34}}{d_{12}}\left[\dfrac{1}{3} + \dfrac{d_{13}d_{23}}{(d_{12} + d_{13} + d_{23})d_{12}}\right] \\[3mm] k_{2n} = \dfrac{1}{2}\dfrac{Et}{(1-v^2)}\dfrac{h_{15}}{d_{23}}\left[\dfrac{1}{3} + \dfrac{d_{12}d_{13}}{(d_{12} + d_{13} + d_{23})d_{23}}\right] \\[3mm] k_{2s} = \dfrac{1}{2}\dfrac{Et}{2(1+v)}\dfrac{h_{15}}{d_{23}}\left[\dfrac{1}{3} + \dfrac{d_{12}d_{13}}{(d_{12} + d_{13} + d_{23})d_{23}}\right] \\[3mm] k_{3n} = \dfrac{1}{2}\dfrac{Et}{(1-v^2)}\dfrac{h_{26}}{d_{13}}\left[\dfrac{1}{3} + \dfrac{d_{12}d_{23}}{(d_{12} + d_{13} + d_{23})d_{13}}\right] \\[3mm] k_{3s} = \dfrac{1}{2}\dfrac{Et}{2(1+v)}\dfrac{h_{26}}{d_{13}}\left[\dfrac{1}{3} + \dfrac{d_{12}d_{23}}{(d_{12} + d_{13} + d_{23})d_{13}}\right] \\[3mm] K_p^{xy} = \dfrac{1}{3}\dfrac{\mu Et}{2(1-v^2)} \\[3mm] K_s^{xy} = \dfrac{1}{3}\dfrac{Et}{4(1+v)} \end{cases} \quad (16)$$

For plane strain condition, the equations are still valid by considering unit thickness and replacing elastic modules E and Poisson's ratio v with E_2 and v_2.

$$\begin{cases} E_2 = E/(1-v^2) \\ v_2 = v/(1-v) \\ t = 1 \end{cases} \quad (17)$$

2.4. Failure criterion

For macroscopic damage, tensile failure can be modeled by Rankine criterion and tangential failure can be modeled by Mohr–Coulomb criterion as

$$\begin{cases} \text{If } -F_n \geq \sigma_t A_c \\ \quad F_n = F_s = 0, \quad \sigma_t = c = 0 \\ \text{If } F_s \geq F_n \tan(\phi) + c A_c \\ \quad F_s = F_n \tan(\phi), \quad \sigma_t = c = 0 \end{cases} \quad (18)$$

where A_c denotes equivalent contact area, σ_t, c and ϕ are tensile strength, cohesion and inner friction angle, respectively. F_n and F_s are the normal and tangential contact forces, obtained by

$$\begin{cases} F_n(t + \Delta t) = F_n(t) - k_n \, \Delta d_n \\ F_s(t + \Delta t) = F_s(t) - k_s \, \Delta d_s \end{cases} \quad (19)$$

in which k_n and k_s denote normal and tangential contact stiffness, Δd_n and Δd_s are normal and tangential relative displacement increment, Δt denotes time increment.
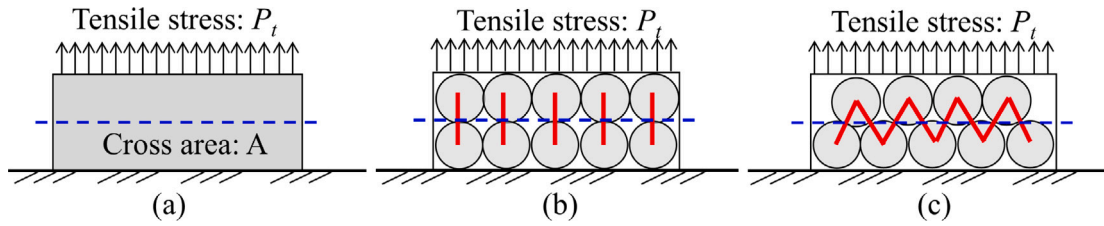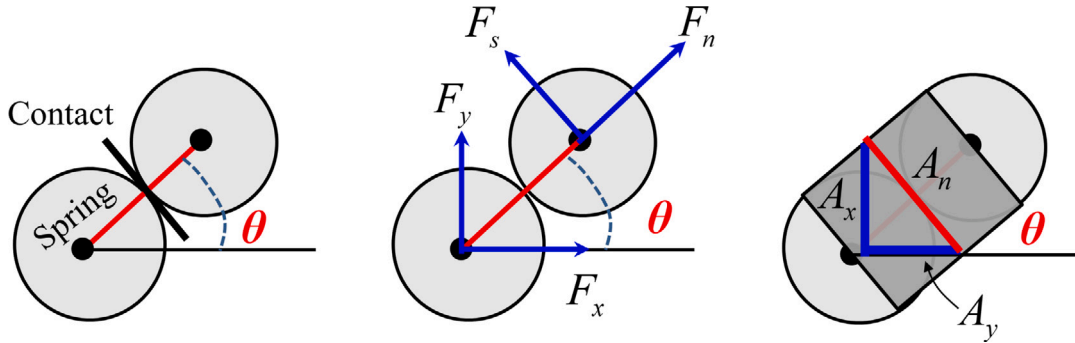
Fig. 5. Three tensile models.

Fig. 6. Local and global spring forces and contact areas.

In the particle–spring system, the failure of springs can happen along normal and tangential directions. However, unlike the continuous media, there is no clear "cross sectional area" in particle–spring system. Herein, we take 2D tensile models shown in Fig. 5 for an example where there are two different particle models comparing to the original continuous model. The tensile stress on the top side is P_t, the tensile strength is σ_t, The cross sectional area of the original continuous model is A.

For continuous model, when P_t reaches σ_t tensile failure will happen. Correspondingly, for the particle–spring models, the external force F_{ext} is

$$F_{ext} = P_t A \tag{20}$$

By decomposing F_{ext} along x and y directions. The horizontal and vertical spring forces on the cross section are

$$\sum_{i=1}^{N} F_x^i = 0 \quad \sum_{i=1}^{N} F_y^i = F_{ext} \tag{21}$$

where F_x^i and F_y^i denote the spring force of the ith spring along x and y directions, N denotes the total number of springs cut by the cross section. In Fig. 5(b), $N = 5$, and in Fig. 5(c), $N = 8$.

Assuming the projection of spring force and the contact area of each spring to the cross section are the same, the vertical force component for each spring on cross section can be determined by

$$F_y = F_{ext}/N \tag{22}$$

For each spring on cross section, F_y is obtained in the local coordinate system as

$$F_y = F_n \sin\theta + F_s \cos\theta \tag{23}$$

where F_n and F_s denote normal and tangential components of the spring forces in local coordinate system, θ denotes included angle between spring and cross section, see Fig. 6.

Similarly for each spring, the projected contact area A_y on the cross section can be calculated by

$$A_y = A/N \tag{24}$$

and the exact contact area of spring A_n (see Fig. 6) can be calculated by

$$A_n = \frac{A_y}{\sin\theta} = \frac{A}{N\sin\theta} \tag{25}$$

Based on Eqs. (20), (22), (23) and (25), following relation is obtained

$$F_n \sin\theta + F_s \cos\theta = P_{ext} A_n \sin\theta, \tag{26}$$

leading to

$$P_{ext} = \frac{F_n \sin\theta + F_s \cos\theta}{A_n \sin\theta} = \sigma_n + \sigma_s \cot\theta \tag{27}$$

where σ_n and σ_s denote the normal and shear stresses of each spring.

Based on Eq. (27), if $\theta < \pi/2$, such as case shown in Fig. 5(c), the tensile stress of spring is smaller than external stress as $P_n < P_{ext}$. Hence the tensile failure of springs will be delayed. Only when $\theta = \pi/2$, such as case shown in Fig. 5(b), $P_n = P_{ext}$. In other words, mostly the failure of springs will be delayed. Aiming at solving this problem, a new failure criterion based on particle stress is introduced. For each particle p the stress tensor σ_{ij} is obtained by

$$\sigma_{ij} = \frac{-1}{V^{(p)}} \sum_{N_c} \left| x_i^{(c)} - x_i^{(p)} \right| n_i^{(c,p)} F_j^{(c)} \tag{28}$$

where $V^{(p)}$ is the volume of particle p, N_c is the particle contact number, $x_i^{(p)}$ is the position of particle centroid, $x_i^{(c)}$ and $F_j^{(c)}$ are the location and force acting at the contact point, $n_i^{(c,p)}$ is the unit normal vector pointed from the particle centroid to the contact location. For a spring connecting two particles, the stress is the mean value of the stresses of the two particles as

$$\sigma_{ij}^c = \frac{\sigma_{ij}^{p1} + \sigma_{ij}^{p2}}{2} \tag{29}$$

where P1 and P2 denote two connected particles.

With the stress tensor of the spring, three principal stress components σ_1, σ_2 and σ_3 are computed first, then the 3D Mohr–Coulomb model with tensile cutoff is adopted for evaluating the failure status. In the iteration step, when Eq. (30) is fulfilled, tensile failure will happen. Otherwise, if Eq. (31) is fulfilled, shear failure will happen.

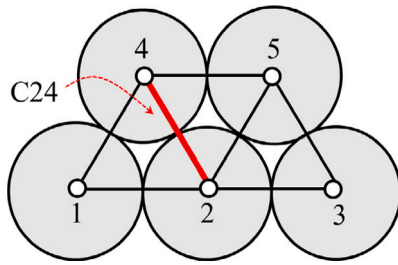$$\begin{cases} \sigma_1 > \sigma_t & and \\ \frac{\sigma_1 \varepsilon_1 d}{2} > G_{ft} \end{cases} \tag{30}$$

Fig. 7. Removing of bond and unconventional springs.

$$\begin{cases} -\sigma_3 > -\sigma_1 \tan^2(\frac{\pi}{4}+\frac{\phi}{2})+2c\tan(\frac{\pi}{4}+\frac{\phi}{2}) \quad and \\ (\sigma_1-\sigma_3)(\varepsilon_1-\varepsilon_3)d > G_{fc} \end{cases} \tag{31}$$

where, ε_1 and ε_3 are maximal and minimal principal strain, G_{ft} and G_{fc} denote tensile and shear fracture energy, and d means the distance of the two contact particles.

ε_1 and ε_3 are expressed as

$$\begin{cases} \varepsilon_1 = \frac{1}{E}\left[\sigma_1 - v(\sigma_2+\sigma_3)\right] \\ \varepsilon_3 = \frac{1}{E}\left[\sigma_3 - v(\sigma_1+\sigma_2)\right] \end{cases} \tag{32}$$

According to Eqs. (30) and (31), only when the strength criterion and energy release rate criterion are met at the same time, the particle bond will break. Once the particle–spring breaks, the tensile strength and cohesion of the contact pair will be set to zero. Subsequently, conventional Coulomb slipping model will be introduced as

$$\begin{cases} If \quad -F_n \geq 0, \quad then \quad F_n = F_s = 0 \\ If \quad F_s < F_n \times \tan(\phi), \quad then \quad F_s = F_n = 0 \\ If \quad F_s \geq F_n \times \tan(\phi), \quad then \quad F_s = F_n \times \tan(\psi) \end{cases} \tag{33}$$

where, ϕ is the static friction angle, ψ is the sliding friction angle.

Besides, when the spring connecting two particles fails, the unconventional springs refer to this connection will also be removed. For example, see Fig. 7, if the spring C24 fails, the unconventional springs inside triangles 1-2-4 and 2-4-5 will be removed consequently.

2.5. Calculation cycle

Incremental explicit solution approach is adopted in particle–spring method, and the calculation cycle is a time stepping algorithm that requires the repeated application of the law of motion to each particle, constitutive laws to particle bonds and particle contacts, and a contact detection scheme to the particles whose contact bonds were totally broken. The calculation cycle is illustrated in Fig. 8. At beginning of each time step, the law of motion is applied to each particle to update its velocity, displacement and position based on the resultant force. Next, if all bonds of the particle are failed completely, the contact searching scheme is executed for this particle based on the newest particle position. Then, the particle bond forces and particle contact forces are computed based on the constitutive laws. At last, the resultant force for each particle is computed based on the bond forces, contact forces and external forces acting on the particle.

3. Numerical studies

3.1. Comparisons between the FEM and particle–spring models

A domain with size (18 cm × 17.32 cm) is shown in Fig. 9, which is discretized into 190 triangle elements. Its bottom side is fixed and its top side is subjected to 1 MPa compression stress. The material properties are: density $\rho = 2500$ kg/m^3, Young's modulus $E = 38$ GPa, Poisson's ratio is $v = 0.23$. Plane strain condition is considered.

Considering the elastic responses, the horizontal displacement contours obtained by conventional FEM and particle–spring models are shown in Fig. 10, indicating agreeable results.
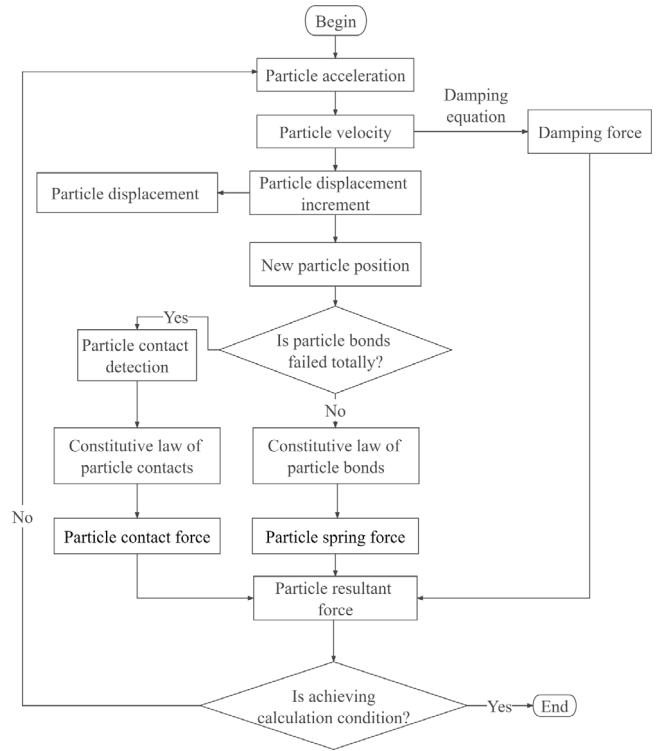

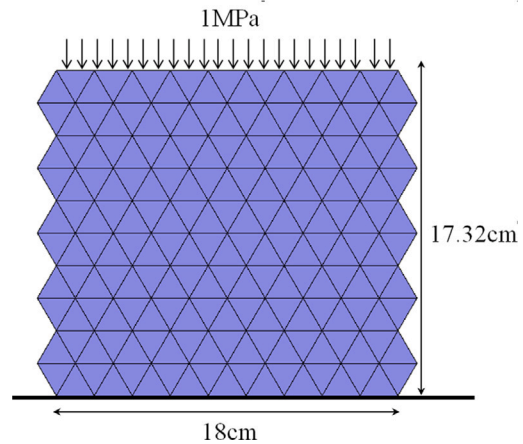Fig. 8. Calculation cycle for particle–spring method.

Fig. 9. Numerical model for elastic test.

3.2. Models considering different particle distributions

For testing the numerical robustness of the proposed model considering different particle distributions, a rectangular numerical model with size 10 cm × 20 cm is used, see Fig. 11. The bottom side is fixed along vertical direction, and a uniform compressive stress 1 MPa is applied on the top side. Plane strain condition is assumed, and the mechanical parameters are the same as those used in the last example (see Section 3.1).

Five different triangular meshes are used for generating particles, see Fig. 12. The errors of Young's modulus E_2 and Poisson's ratio v_2 obtained with the particle–spring models are listed in Table 1.

Where the values of E_2 and v_2 are calculated by

$$\begin{aligned} E_2 &= \sigma_c/(\bar{v}_t/L) \\ v_2 &= |(\bar{u}_r - \bar{u}_l)/\bar{v}_t| \end{aligned} \tag{34}$$

(a) X-displacement of FEM
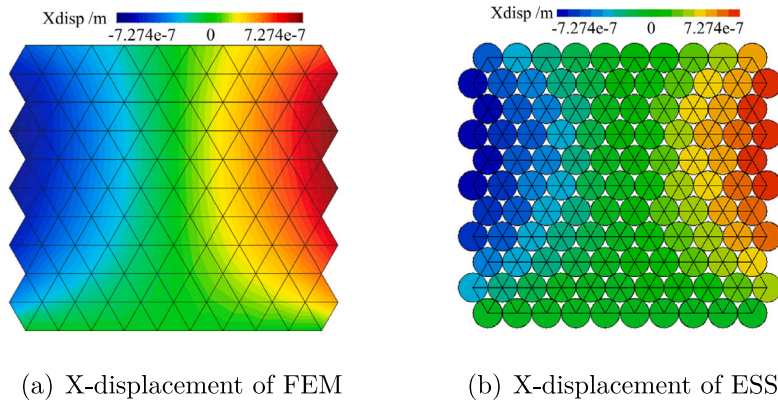

(b) X-displacement of ESS

Fig. 10. Displacement contour comparison between FEM and particle–spring model.
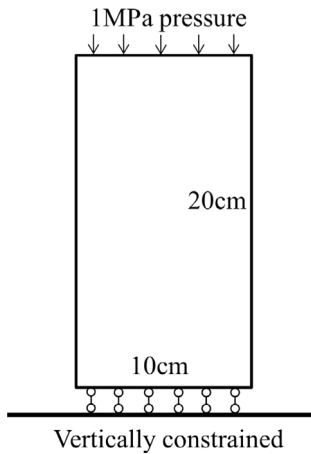

Fig. 11. Numerical model for testing different particle distributions.

Table 1
Errors of Young's modulus and Poisson's ratio obtained by the particle–spring model.

Types	Mesh 1	Mesh 2	Mesh 3	Mesh 4	Mesh 5
Error of E_2	0.22%	0.48%	0.82%	0.18%	−2.09%
Error of ν_2	0.04%	−1.38%	−1.80%	−2.71%	−3.89%

Table 2
Material parameters of the rock specimen.

Density kg/m³	Elastic modulus GPa	Poisson's ratio –	Tensile strength MPa
2500	30	0.2	1

where $\sigma_c = 1$ MPa denotes compressive stress applied on top side, $h = 0.2$ m is the height of the model, $\bar{v}_t$ is the average vertical displacement on the top side and $\bar{u}_r$ and $\bar{u}_l$ denote average horizontal displacements on the right and left sides. The results indicate that even in the worst case (case 5) the errors provided by our model is less than 4%.

3.3. Pulling test

Dog-boned shaped pulling tests are considered for testing the tensile failure processes of rock specimen, see the model shown in Fig. 13. 5984 particles are used for this example. The material properties are provided in Table 2. And the parameters of tensile fracture energy and shear fracture energy in this conditions are 0.

For comparisons, we consider four cases in this example as:

Table 3
Material parameters of the rock specimen.

Density kg/m³	Elastic modulus GPa	Poisson's ratio –	Cohesive strength MPa	Inner friction angle °
2500	30	0.2	3	30

- Case 1: using the proposed particle–spring model with the new failure criterion;
- Case 2: using the proposed particle–spring model with the conventional failure criterion;
- Case 3: using conventional particle discrete element model;
- Case 4: using FEM model with Rankine failure criterion;

The force–displacement curves are shown in Fig. 14. In the linear elastic stage, the proposed model provides agreeable force–displacement responses comparing to the FEM results, while the conventional particle discrete element model underestimates the stiffness of the structure, which also underestimates the peak load. Considering the peak stress, the FEM model with Rankine failure criterion obtains the best results while the error of our proposed model is around 12%. However, we would like to emphasize that the new failure criterion are much better than the conventional one, which will get delayed failure processes and greatly overestimate the peak load, see Section 2.4. The failure patterns are shown in Fig. 15.

Considering the error of the proposed model, we believe it is mainly caused by the non-uniform distribution of the particles, which results into stress concentration, see Eq. (29). When using pure brittle failure model, stress concentration will cause early breakage of some springs and underestimate the peak loads. Hence we consider case 5 as: building the particle–spring model with the FEM nodes and using the proposed particle–spring model with the new failure criterion. The force–displacement curves of cases 1, 4, and 5 are shown in Fig. 16, indicating that the result is greatly improved when building particle based on FEM nodes, which can alleviate stress concentration caused by non-uniform particle distribution.

3.4. Compression test

Uniaxial compression test is considered in this section, see the model shown in Fig. 17. 2984 nodes and 5768 triangular elements are built in the FEM model, which producing 2984 particles for the proposed particle–spring model. The material properties are provided in Table 3.

Unlike the brittle tensile failure in which case the damaged springs are removed and there is no force acting on the corresponding particles, for compression-shear failure interlock and sliding friction effects will appear inside particles after cracking. Here, the interlock effects are
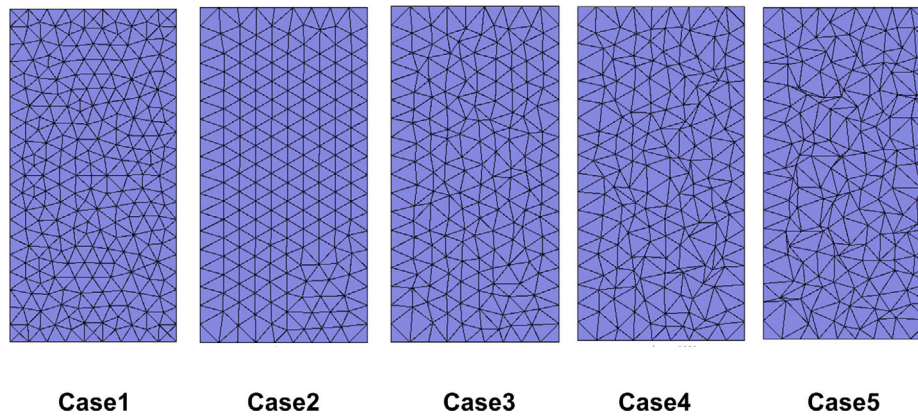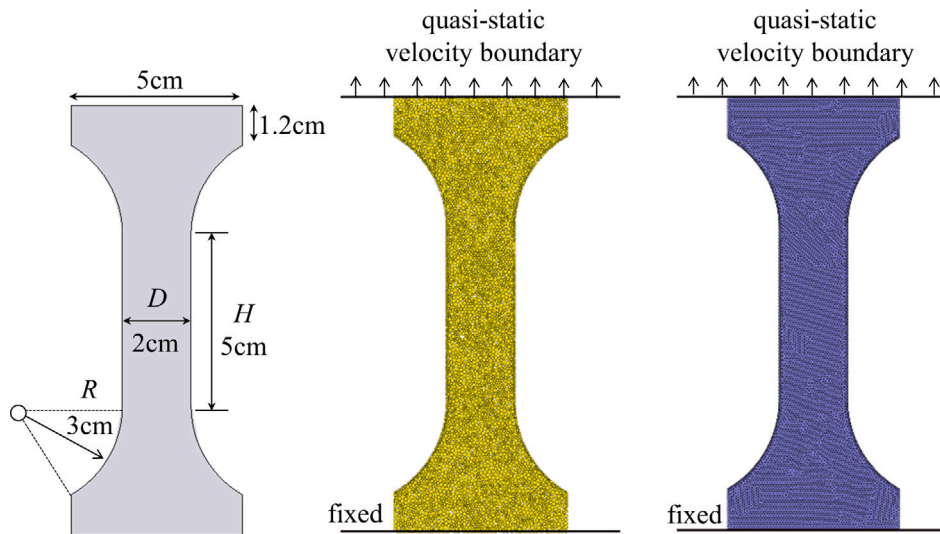
Fig. 12. Five different meshes.

Fig. 13. Numerical models for direct tensile test.
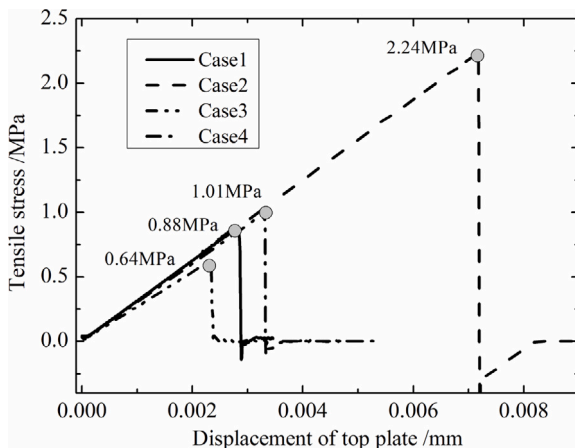

Fig. 14. Force–displacement curves of the pulling test.

mainly controlled by the particle distributions, and the sliding friction effects are controlled by the sliding friction angle ψ. Generally, the value of sliding friction angle is different from the inner friction angle. And the parameters of tensile fracture energy and shear fracture energy in this conditions are 0. We consider different sliding friction angles and set 6 cases as

- Case 1: the proposed model with $\psi = 10°$;
- Case 2: the proposed model with $\psi = 15°$;
- Case 3: the proposed model with $\psi = 20°$;
- Case 4: the proposed model with $\psi = 25°$;
- Case 5: the proposed model with $\psi = 30°$;
- Case 6: FEM model with the friction angle $30°$;

where for case 6 the friction angle is a macroscopic property. The obtained stress–strain curves are shown in Fig. 18. Similar to the results of the pulling test, the stress–strain curves of all cases at the elastic stages are almost the same. The peak load of Case 6 agrees well with the analytical results as

$$\sigma_c = 2c \tan(\frac{\pi}{4}+\frac{\phi}{2}) \approx 10.39 \text{ MPa} \tag{35}$$

The relationship between sliding friction angles and the peak loads are shown in Fig. 19, which indicates the sliding friction angle corresponds to 10.39 MPa is $\psi = 17° \leq 30°$. As mentioned before, the sliding friction angle of our particle–spring model is used for describing the sliding effects between two particles after compression-shear failure. However, the friction angle in FE model is a macroscopic parameter, which is the combination of microscopic sliding friction angle and microscopic interlock between particles. So, for the same peak load, the sliding friction angle in our model is smaller than the one in FE model.
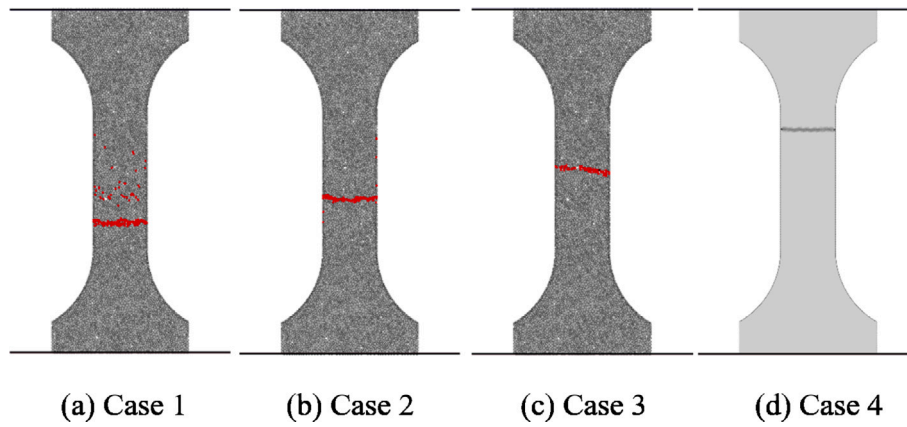
Fig. 15. Failure patterns of different cases (in (a) (c), gray points represent particles and red points represent broken springs; in (d), light gray parts represent intact elements, and heavy gray parts represent broken elements). (For interpretation of the references to color in this figure legend, the reader is referred to the web version of this article.)
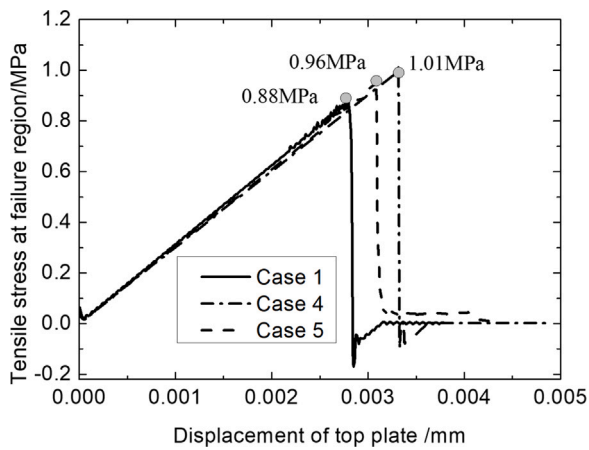

Fig. 16. Force–displacement curves of particle models comparing to FEM results (case 1 and case 4 are the same as those shown in Fig. 14).
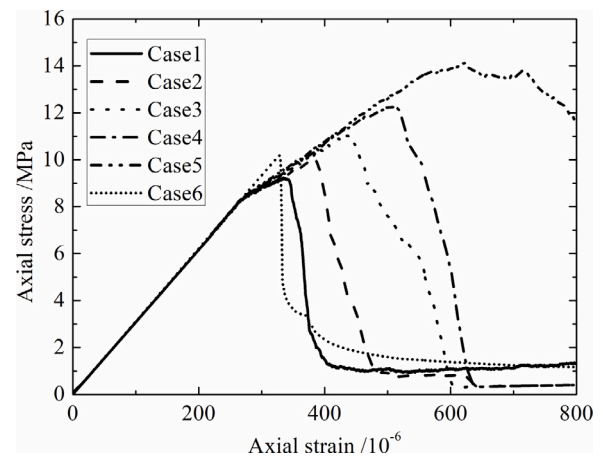

Fig. 18. Force–displacement curves of the proposed particle–spring model comparing to the FEM model.
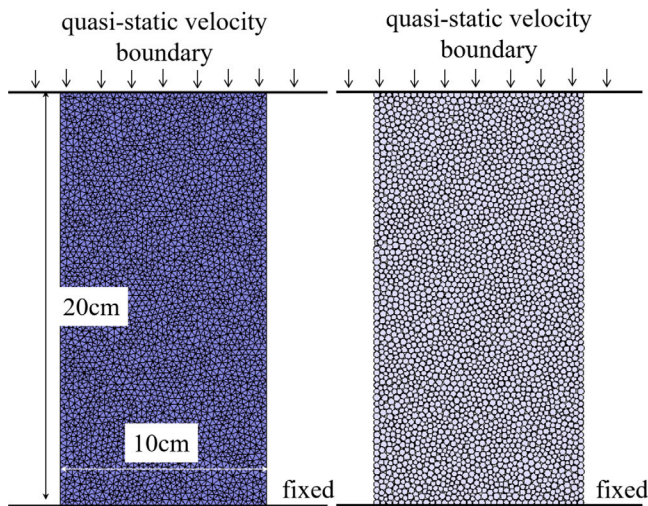

Fig. 17. Numerical models for the compression test.
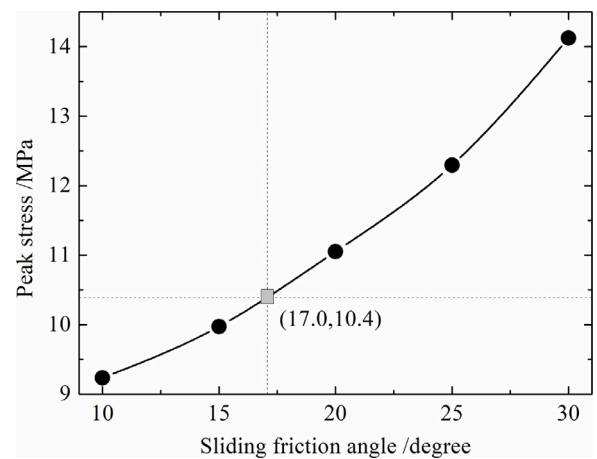

Fig. 19. Relationship between peak stress and sliding friction angle.

For the proposed particle–spring model, the equivalent shear strain for each particle is defined as

$$\bar{\gamma} = \frac{1}{N_c} \sum_{i=1}^{N_c} u_s^i / R \tag{36}$$

where $\bar{\gamma}$ is the equivalent shear strain for one particle, N_c is the total contact number, u_s^i / R denotes the shear displacement of contact i, and R is the radius of particle. The equivalent shear strains after peak point are shown in Fig. 20. It can be found that with the increase of the sliding friction angle, the angle between the damaging surfaces and the x-axis increases.
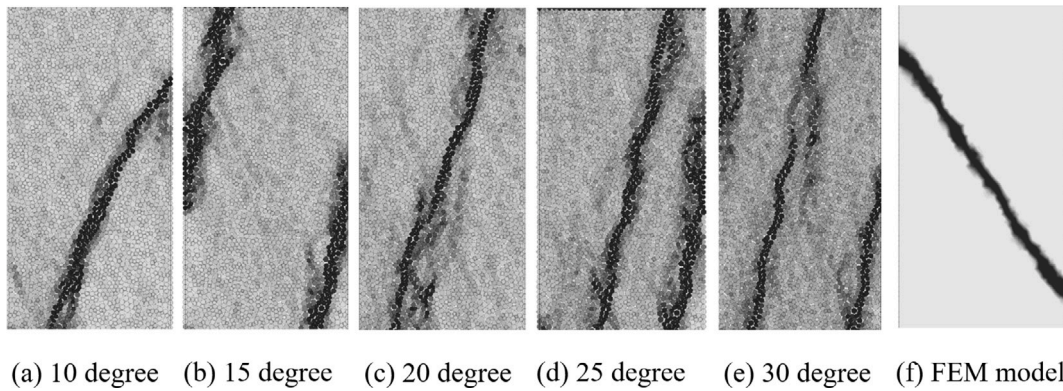
Fig. 20. The obtained equivalent shear strain of cases 1 to 6.

4. Conclusions

In this work, we proposed a simple particle–spring method for capturing the continuum–discontinuous behavior of brittle materials. The method introduces several springs with physical backgrounds for the particle system. By building the equivalence between the particle–spring and a corresponding FEM systems, the stiffness matrix of the particle–spring system can be easily obtained. Moreover, a new failure criterion for the particle–spring system is proposed, taking into account not only tensile but also compression-shear failures. In several numerical example, the method provides agreeable results comparing the results obtained the FEM method, indicating its effectiveness and robustness.

Declaration of competing interest

The authors declare that they have no known competing financial interests or personal relationships that could have appeared to influence the work reported in this paper.

Code availability

The code is custom code, if there is any question, please contact the corresponding author.

References

[1] de Borst R. Some recent issues in computational failure mechanics. Internat J Numer Methods Engrg 2001;52:63–95.

[2] Wu J-Y, Cervera M. On the equivalence between traction- and stress-based approaches for the modeling of localized failure in solids. J Mech Phys Solids 2015;82:137–63.

[3] Zhang Y, Gao Z, Li Y, Zhuang X. On the crack opening and energy dissipation in a continuum based disconnected crack model. Finite Elem Anal Des 2020;170. http://dx.doi.org/10.1016/j.finel.2019.103333.

[4] Cervera M, Wu J-Y. On the conformity of strong, regularized, embedded and smeared discontinuity approaches for the modeling of localized failure in solids. Int J Solids Struct 2015;71:19–38.

[5] Wu J-Y, Nguyen VP. A length scale insensitive phase-field damage model for brittle fracture. J Mech Phys Solids 2018;119:20–42.

[6] Wu J-Y. Robust numerical implementation of non-standard phase-field damage models for failure in solids. Comput Methods Appl Mech Engrg 2018;340:767–97.

[7] Wu J-Y. A unified phase-field theory for the mechanics of damage and quasi-brittle failure. J Mech Phys Solids 2017;103:72–99.

[8] Cervera M, Chiumenti M. Smeared crack approach: back to the original track. Int J Numer Anal Methods Geomech 2006;30:1173–99.

[9] Areias P, Rabczuk T, Dias-da-Costa D. Element-wise fracture algorithm based on rotation of edges. Eng Fract Mech 2013;110:113–37.

[10] Areias P, Rabczuk T. Steiner-point free edge cutting of tetrahedral meshes with applications in fracture. Finite Elem Anal Des 2017;132:27–41.

[11] Belytschko T, Chen H, Xu J, Zi G. Dynamic crack propagation based on loss of hyperbolicity with a new discontinuous enrichment. Internat J Numer Methods Engrg 2003;58:1873–905.

[12] Song J, Belytschko T. Cracking node method for dynamic fracture with finite elements. Internat J Numer Methods Engrg 2009;77:360–85.

[13] Matsuki K, Nakama S, Sato T. Estimation of regional stress by FEM for a heterogeneous rock mass with a large fault. Int J Rock Mech Min Sci 2009;46(1):31–50.

[14] Zhou X-P, Chen J-W, Berto F. XFEM based node scheme for the frictional contact crack problem. Comput Struct 2020;231:106221.

[15] He B, Zhuang X. Modeling hydraulic cracks and inclusion interaction using XFEM. Undergr Space 2018;3(3):218–28.

[16] Yang Y, Sun G, Zheng H. Stability analysis of soil-rock-mixture slopes using the numerical manifold method. Eng Anal Bound Elem 2019;109:153–60.

[17] Xu D, Wu A, Li C. A linearly-independent higher-order extended numerical manifold method and its application to multiple crack growth simulation. J Rock Mech Geotech Eng 2019;11(6):1256–63.

[18] Wu Z, Xu X, Liu Q, Yang Y. A zero-thickness cohesive element-based numerical manifold method for rock mechanical behavior with micro-voronoi grains. Eng Anal Bound Elem 2018;96:94–108.

[19] Zheng H, Xu D. New strategies for some issues of numerical manifold method in simulation of crack propagation. Internat J Numer Methods Engrg 2014;97:986–1010.

[20] Zheng H, Liu F, Du X. Complementarity problem arising from static growth of multiple cracks and MLS-based numerical manifold method. Comput Methods Appl Mech Engrg 2015;295:150–71.

[21] Saloustros S, Pelà L, Cervera M, Roca P. Finite element modelling of internal and multiple localized cracks. Comput Mech 2017;59:299–316.

[22] Saloustros S, Cervera M, Pelà L. Tracking multi-directional intersecting cracks in numerical modelling of masonry shear walls under cyclic loading. Meccanica 2018;53(7):1757–76.

[23] Cervera M, Pela L, Clemente R, Roca P. A crack-tracking technique for localized damage in quasi-brittle materials. Eng Fract Mech 2010;77:2431–50.

[24] Zhang Y, Lackner R, Zeiml M, Mang H. Strong discontinuity embedded approach with standard SOS formulation: Element formulation, energy-based crack-tracking strategy, and validations. Comput Methods Appl Mech Engrg 2015;287:335–66.

[25] Zhang Y, Zhuang X. Cracking elements: a self-propagating strong discontinuity embedded approach for quasi-brittle fracture. Finite Elem Anal Des 2018;144:84–100.

[26] Zhang Y, Zhuang X. Cracking elements method for dynamic brittle fracture. Theor Appl Fract Mech 2019;102:1–9.

[27] Zhang Y, Mang HA. Global cracking elements: a novel tool for Galerkin-based approaches simulating quasi-brittle fracture. Internat J Numer Methods Engrg 2020;121:2462–80.

[28] Mu L, Zhang Y. Cracking elements method with 6-node triangular element. Finite Elem Anal Des 2020;177:103421.

[29] Zhang Y, Huang J, Yuan Y, Mang HA. Cracking elements method with a dissipation-based arc-length approach. Finite Elem Anal Des 2021;195:103573.

[30] Oliver J, Huespe A. Continuum approach to material failure in strong discontinuity settings. Comput Methods Appl Mech Engrg 2004;193:3195–220.

[31] Meschke G, Dumstorff P. Energy-based modeling of cohesive and cohesionless cracks via X-FEM. Comput Methods Appl Mech Engrg 2007;196:2338–57.

[32] Saloustros S, Cervera M, Pelà L. Challenges, tools and applications of tracking algorithms in the numerical modelling of cracks in concrete and masonry structures. Arch Comput Methods Eng 2019;26:961–1005.

[33] Areias P, Msekh M, Rabczuk T. Damage and fracture algorithm using the screened Poisson equation and local remeshing. Eng Fract Mech 2016;158:116–43.

[34] Areias P, Reinoso J, Camanho P, Rabczuk T. A constitutive-based element-by-element crack propagation algorithm with local mesh refinement. Comput Mech 2015;56:291–315.

[35] Linder C, Raina A. A strong discontinuity approach on multiple levels to model solids at failure. Comput Methods Appl Mech Engrg 2013;253:558–83.

[36] Linder C, Armero F. Finite elements with embedded branching. Finite Elem Anal Des 2009;45:280–93.

[37] Zhuang X, Augarde C, Mathisen K. Fracture modeling using meshless methods and level sets in 3D: framework and modeling. Internat J Numer Methods Engrg 2012;92:969–98.

[38] Zhuang X, Augarde C, Bordas S. Accurate fracture modelling using meshless methods, the visibility criterion and level sets: Formulation and 2D modelling. Internat J Numer Methods Engrg 2011;86:249–68.

[39] Rabczuk T, Zi G. A meshfree method based on the local partition of unity for cohesive cracks. Comput Mech 2007;39:743–60.

[40] Bordas S, Rabczuk T, Zi G. Three-dimensional crack initiation, propagation, branching and junction in non-linear materials by an extended meshfree method without asymptotic enrichment. Eng Fract Mech 2008;75:943–60.

[41] Rabczuk T, Belytschko T. Cracking particles: a simplified meshfree method for arbitrary evolving cracks. Internat J Numer Methods Engrg 2004;61:2316–43.

[42] Rabczuk T, Belytschko T. A three-dimensional large deformation meshfree method for arbitrary evolving cracks. Comput Methods Appl Mech Engrg 2007;196:2777–99.

[43] Rabczuk T, Bordas S, Zi G. On three-dimensional modelling of crack growth using partition of unity methods. Comput Struct 2010;88:1391–411.

[44] Rabczuk T, Zi G, Bordas S, Nguyen-Xuan H. A simple and robust three-dimensional cracking-particle method without enrichment. Comput Methods Appl Mech Engrg 2010;199:2437–55.

[45] Nikolić M, Karavelić E, Ibrahimbegovic A, Miščević P. Lattice element models and their peculiarities. Arch Comput Methods Eng 2018;25(3):753–84.

[46] Zhao G-F. Developing a four-dimensional lattice spring model for mechanical responses of solids. Comput Methods Appl Mech Engrg 2017;315:881–95.

[47] Jiang C, Zhao G-F, Khalili N. On crack propagation in brittle material using the distinct lattice spring model. Int J Solids Struct 2017;118–119:41–57.

[48] Han F, Lubineau G, Azdoud Y. Adaptive coupling between damage mechanics and peridynamics: A route for objective simulation of material degradation up to complete failure. J Mech Phys Solids 2016;94:453–72.

[49] Li W-J, Zhu Q-Z, Ni T. A local strain-based implementation strategy for the extended peridynamic model with bond rotation. Comput Methods Appl Mech Engrg 2020;358:112625.

[50] Yu H, Chen X, Sun Y. A generalized bond-based peridynamic model for quasi-brittle materials enriched with bond tension–rotation–shear coupling effects. Comput Methods Appl Mech Engrg 2020;372:113405.

[51] Zhang Y, Yang X, Wang X, Zhuang X. A micropolar peridynamic model with non-uniform horizon for static damage of solids considering different nonlocal enhancements. Theor Appl Fract Mech 2021;113:102930.

[52] Ren H, Zhuang X, Cai Y, Rabczuk T. Dual-horizon peridynamics. Internat J Numer Methods Engrg 2016;108(12):1451–76.

[53] Ren H, Zhuang X, Rabczuk T. Dual-horizon peridynamics: A stable solution to varying horizons. Comput Methods Appl Mech Engrg 2017;318:762–82.

[54] Rabczuk T, Ren H, Zhuang X. A nonlocal operator method for partial differential equations with application to electromagnetic waveguide problem. Comput Mater Continua 2019;59. Nr. 1.

[55] Ren H, Zhuang X, Rabczuk T. A nonlocal operator method for solving partial differential equations. Comput Methods Appl Mech Engrg 2020;358:112621.

[56] Hillerborg A, Modéer M, Petersson P-E. Analysis of crack formation and crack growth in concrete by means of fracture mechanics and finite elements. Cem Concr Res 1976;6(6):773–81.

[57] Cundall PA, Strack OD. A discrete numerical model for granular assemblies. Geotechnique 1979;29(1):47–65.

[58] Potyondy DO, Cundall P. A bonded-particle model for rock. Int J Rock Mech Min Sci 2004;41(8):1329–64.

[59] Zhang Qingbo FC, Jie W. Study of deformable block discrete element method based on SEM. Rock Soil Mech 2013.

[60] Jie W, Shihai L. Continuous-discontinuous coupling model for crack initiation and propagation analysis. In: International conference on airworthiness & fatigue-icsaels. 2013.

[61] Meguro K, Hakuno M. Fracture analyses of concrete structures by the modified distinct element method. Doboku Gakkai Ronbunshu 1989;1989(410):113–24.

[62] Meguro K, Tagel-Din H. Applied element method for structural analysis theory and application for linear materials. Doboku Gakkai Ronbunshu 2000;2000(647):31–45.